Supplementary Information for

Phonon-Suppressed Auger Trapping of Charge Carriers in Defective Two-Dimensional Transition Metal Dichalcogenides

Linqiu Li,[1,#] Ming-Fu Lin,[2,#] Xiang Zhang,[3] Alexander Britz,[2,4] Aravind Krishnamoorthy,[5] Ruru Ma,[5] Rajiv K. Kalia,[5] Aiichiro Nakano,[5] Priya Vashishta,[5] Pulickel Ajayan,[3] Matthias C. Hoffmann,[2] David M. Fritz,[2] Uwe Bergmann,[4*] Oleg V. Prezhdo,[1,6*]

[1]Department of Chemistry, University of Southern California, Los Angeles, CA 90089

[2]Linac Coherent Light Source, SLAC National Accelerator Laboratory, Menlo Park, CA 94025

[3]Department of Materials Science and Nanoengineering, Rice University, Houston, TX 77005

[4]Stanford PULSE Institute, SLAC National Accelerator Laboratory, Menlo Park, CA 94025

[5]Collaboratory for Advanced Computing and Simulations, Department of Physics &Astronomy, Department of Computer Science, Department of Chemical Engineering & Materials Science, Department of Biological Sciences, University of Southern California, Los Angeles, CA 90089

[6]Department of Physics & Astronomy, University of Southern California, Los Angeles, CA 90089

[#]These two authors contributed equally

[*]Corresponding authors: prezhdo@usc.edu, bergmann@slac.stanford.edu

I. Sample Preparation and Characterization

The $MoTe_2$ thin film was synthesized by tellurizing a Mo film at 700°C for 2 hours in a tube furnace. The Mo film was deposited on a quartz substrate by e-beam evaporation previous to the reaction with Te powders. The as-synthesized $MoTe_2$ film was characterized by Raman spectroscopy and atomic force microscopy (AFM). The Raman spectrum in Figure S1 shows several modes including E_{1g}, A_{1g} , E^1_{2g}, B^1_{2g}, indicating that the $MoTe_2$ film forms the 2H phase. Figure S2 demonstrates that the thickness of the $MoTe_2$ film is around 9 ± 1.1 nm. The detailed sample preparation and characterization can be found in Ref 1[1]. Note that the synthesized $MoTe_2$ is a large area and continuous polycrystalline thin film.

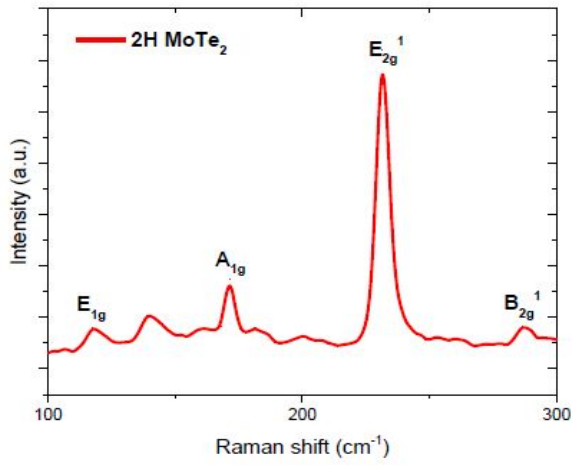

Figure S1. Raman spectrum of the synthetized 9 ± 1.1 nm thick 2H-phase $MoTe_2$ film.

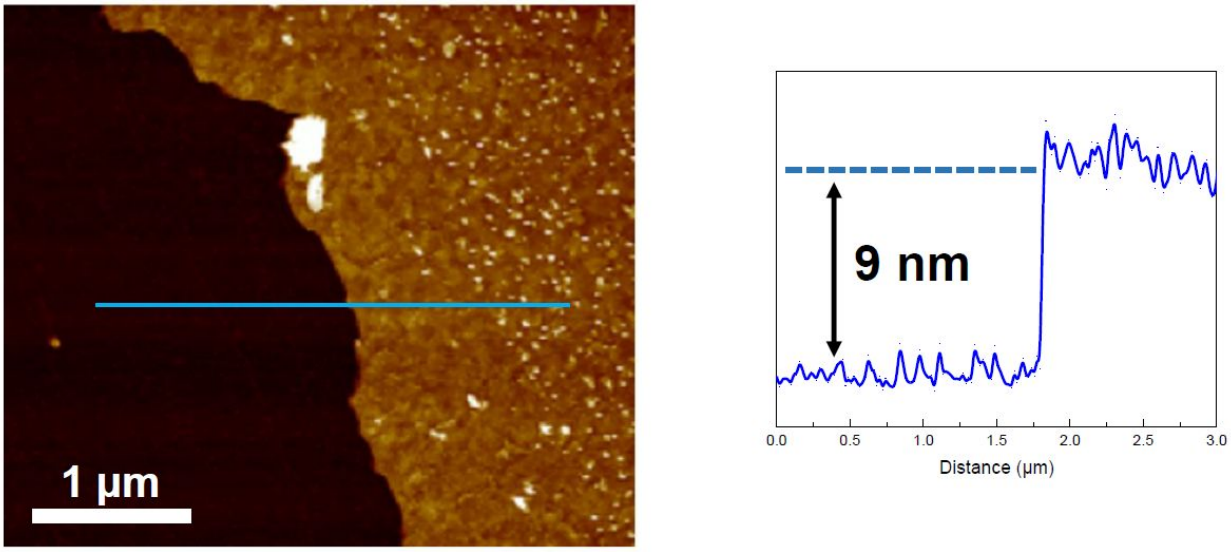

Figure S2. AFM image of the synthetized $MoTe_2$ film, and the height profile along the blue line.

II. Experimental Layout

Figure S3 shows the instrument of the optical pump and terahertz (THz) probe transient absorption spectroscopy. The experiment setup contains a chirp-pulse-amplified Ti:Sapphire femtosecond laser system operated at 1 kHz with central wavelength of 800 nm and pulse duration of ~50 fs. The output of the laser beam is directed to the first 80/20 beam splitter (BS) for the following generation of pump and probe beams. The beam splitter reflects 80% of the near infrared (NIR) for the THz generation. The other 20% of the laser energy is used for the optical pump on the ~9 nm thick $MoTe_2$ to create free carriers and to probe the THz field. The THz pulses are generated by sending an unfocused NIR laser beam through a ZnTe crystal. The produced THz laser is collimated and focused by the first three parabolic mirrors on the sample film. A silicon plate is installed in the beam path to reject the residual 800 nm. After samples, two parabolic mirrors collimate and focus the THz beam on an electric-optic (EO) crystal (110 cut ZnTe), and

modulate the polarization of the incoming 800 nm beam split from a 50/50 beam splitter. After the EO crystal, a quarter waveplate (QW) and a Wollaston prism produce and separate the THz-modulated S/P polarizations of the 800 nm beam, respectively, and the spatially separated 800 nm beams are measured by two independent photodiodes (PD1 and PD2). Two PDs are connected to a lock-in-amplifier with synchronization to a Thorlabs chopper for the final THz field mapping through a scan of translation stage of 800 nm probe beam. For the carrier density variation, a combination of a half-wave plate (HWP) and polarizer is employed to vary the pump fluence on the sample films. The whole apparatus is contained in a small 1-feet-by-2-feet box and is purged with dried air to avoid the water vapor absorption in the THz frequency range.

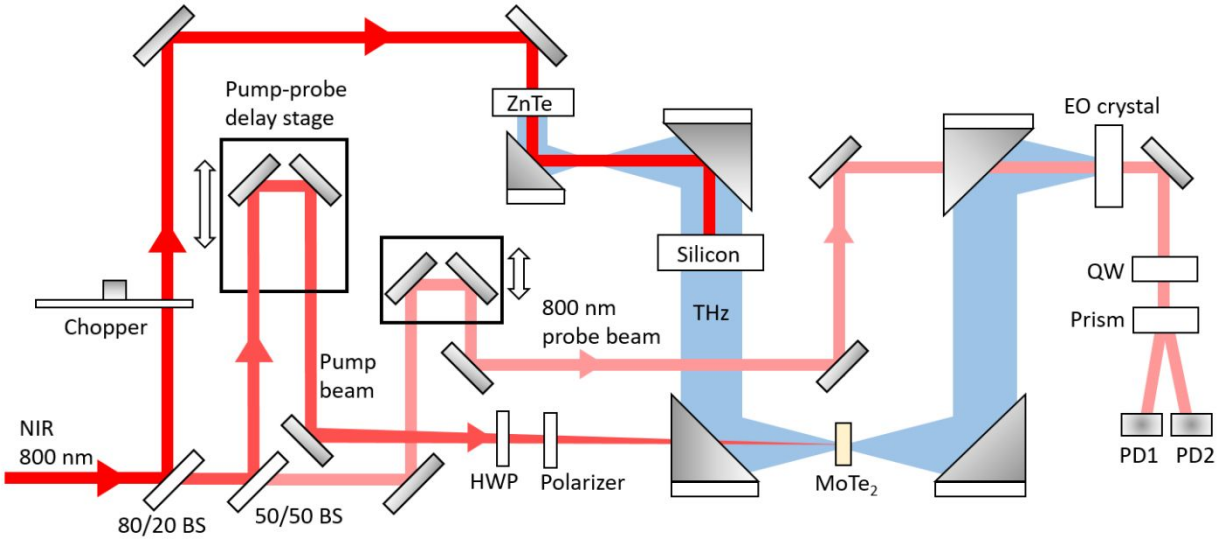

Figure S3. The instrument layout for the optical pump and THz probe transient absorption spectroscopy. BS, HWP, QW, EO and PD represent beam splitter, half-wave plate, quarter waveplate, electric-optics and photodiode, respectively.

III. THz Transient Absorption Acquisition and Data Analysis

At each pump fluence, we repeated the pump-probe delay scan approximately ten times to improve the signal-to-noise ratio. At each pump-probe delay time, the THz field is mapped by the 800 nm beam with ~30 ms accumulation for each point. The time window for electro-optic THz field scan is ~9 ps, corresponding to the spectral resolution of ~0.11 THz. The 2D false color map of the averaged THz field from multiple scans is shown as a function of pump-probe delay time in Figure S4a. In this 2D data, each time-domain THz waveform is Fourier-transformed to the spectral domain, so that the amplitude of the probe spectrum is obtained. From this method, we are able to eliminate the possible phase drift of the THz field due to the laser instability.

In order to obtain the transient absorption spectrum, ΔA, we proceed to the following data reduction procedures. First, the reference spectrum, $S^{ref.}_{(\omega,\,-\,t_{ave.})}$, is obtained by averaging the first five points of the negative delay time. Each transient spectrum is calculated by taking the difference between the reference spectrum and the spectrum at the corresponding delay time, $S_{(\omega,\,t)}$, followed by normalization to the reference spectrum. The calculation of the transient spectrum is shown in Equation S1, where ω and t denote the THz frequency and the pump-probe delay time, respectively. The final 2D color map of the transient absorption spectrum is shown in Figure S4b. The time-resolved kinetics at each pump fluence is obtained by integrating the transient absorption signal in the spectral range from 0.5 THz to 2.3 THz and is shown in Figure 4 in the main text.

$$\Delta A_{(\omega,t)} = \frac{S_{(\omega,t)} - S^{ref.}_{(\omega,\,-\,t_{ave.})}}{S^{ref.}_{(\omega,\,-\,t_{ave.})}} \qquad \text{Equation S1.}$$

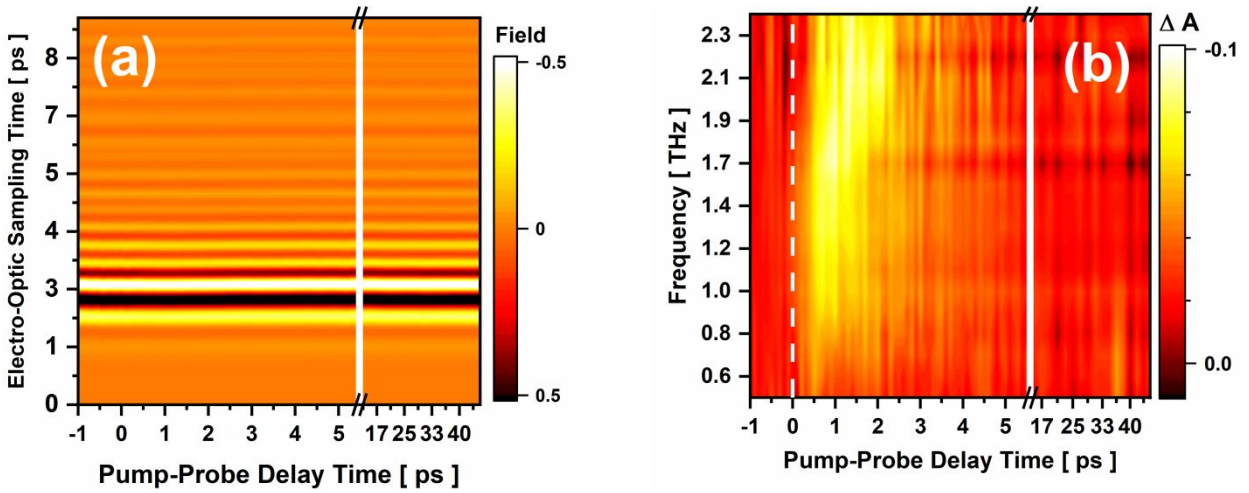

Figure S4. Optical pump and THz probe transient absorption spectroscopy of 2H-phase $MoTe_2$ at carrier density of 4.6×10^{20} cm^{-3}. **(a)** 2D map of 800 nm electro-optic sampling time versus pump-probe delay time. **(b)** 2D map of normalized THz spectral difference versus pump-probe delay time. The normalized spectral difference is calculated according to Equation S1.

IV. Carrier Density Estimation

The carrier density is calculated by estimating the final effective absorption of pulse energy at 800 nm. In this experiment the pump beam is normal incident to the sample surface as shown in Supplementary Figure S5. We assume that each absorbed 800 nm photon creates an electron-hole pair that eventually dissociates into free charge carriers. Here, we use the equations described in **4**(119) and **4**(120) in Supplementary Ref 2[2] that incorporates the complex refractive indices of air, $MoTe_2$ and substrates at 800 nm to calculate the absorption, reflection and transmission without considering the saturation effect due to the pump beam. Next step we consider the saturable absorber effect (Equation S2) to obtain the final effective absorption by the sample at high pump fluences.

$$\alpha = \frac{\alpha_0}{1+\frac{I}{I_0}} \qquad \text{Equation S2.}$$

, where α and α_0 represent the absorption cross sections with and without saturation effect of the pump beam. I and I_s represent the irradiated and saturated peak intensities, respectively. The 800 nm pump pulse duration is approximately 100 fs which gives us the peak intensity in the range from 0.4 to 43 GW/cm^2. The saturation peak intensity of $MoTe_2$ at 800 nm is ~ 217 GW/cm^2.[3] This yields a small correction of the absorption by ~0.1 to 2 % in current pump peak intensity range. The complex indices of refraction for Air, $MoTe_2$ and quartz (sapphire) substrate at 800 nm photon energy are 1.0, 4.62-1.67i and 1.453(1.76), respectively. Table S1 displays the calculation of carrier density using complex indices of refraction and saturable absorber model. Note that the error in the pump beam diameter can be as high as ~50% due to the nonlinearity of CCD pixel of image camera. All the peak fluence is calculated using equation F (mJ/cm2) = $2E/\pi\omega^2$, where E and ω are the pulse energy and beam radius (i.e. $1/e^2$ drop in intensity), respectively. In addition, all the experiments are carried out with samples either on quartz or sapphire substrates which does not show any substrate effect in the decay of carrier relaxation dynamics.

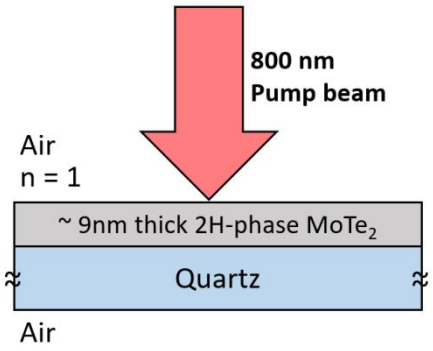

Figure S5. The normal incidence configuration of pump beam relative to the ~9 nm thick $MoTe_2$ thin film on ~ 1 mm thick quartz (or sapphire) substrate.

Table S1. Carrier density estimation using complex indices of refraction and saturable absorber.

Pump beam radius (mm)	Pulse Energy (μJ)	Peak Fluence (mJ/cm^2)	Abs./Refl./ Trans. (%)	Peak power (GW/cm^2)	Effective Abs (%)	Carrier Density (cm^{-3})
1.5	1.35	0.04	13/37/50	0.38	13	1.1E19
1.5	2.8	0.08	19/31/50	0.79	18.9	3.4E19
0.55	0.84	0.21	19/31/50	1.76	18.8	7.5E19
0.55	2.22	0.64	19/31/50	4.67	18.6	1.9E20
0.55	5.42	1.3	19/31/50	11.4	18	4.6E20
0.55	10	2.6	19/31/50	21	17.3	8.2E20
0.55	20.45	5.1	13/37/50	43	10.9	1.0E21

V. Simulation Details

The simulation supercell is obtained through repeating the unit cell of the $MoTe_2$ bilayer 3*3 times. The supercell is a hexagonal structure with the cell constants a=10.73 Å, b=10.73 Å and c=25 Å. A vacuum of 14 Å is placed on the c direction to avoid spurious interactions between adjacent images of the bilayer. All calculations are performed with a cutoff energy of 50 Ry. The Perdew, Burke, and Ernzerhof (PBE) functional is selected to describe the nonlocal exchange-correlation terms, because it provides a practical middle-ground to balance accuracy and computational cost. The projector-augmented wave (PAW) method is chosen to treat interactions between ionic cores and valence electrons. The van der Waals interactions were described by the semiempirical potential introduced by Grimme's in the DFT-D2 method with a 200 a.u. cutoff radius.

The Quantum Espresso program is used to perform geometry optimization, electronic structure calculations and adiabatic molecular dynamics (MD) simulation. The perfect and defective $MoTe_2$ bilayers are fully relaxed at 0 K until the calculated Hellmann-Feynman forces were smaller than 0.05 eV/Å. These optimized structures are used to compute densities of states (DOS) shown in Figure 3 and charge density distributions shown in insets in Figure 4. The DOS were calculated through using a 9×9×1 k-point mesh. Then, the structures are heated to 300 K

through repeated velocity rescaling. Because of thermal fluctuations, the energy gap between the conduction band minimum (CBM) and the shallow trap state (i.e. the trap state close to the CBM) in the defective bilayer $MoTe_2$ narrows down by 25%, (from 0.2 eV to 0.15 eV), while other energy gaps remain similar. After that, a 3 ps adiabatic MD trajectory is computed with a 1 fs nuclear timestep, and the nonadiabatic (NA) coupling matrix elements are calculated along the trajectory. It is important to note that the 3 ps trajectory is sufficient to sample phonon induced fluctuations in the energy levels and NA couplings, because the system is close to harmonic and undergoes oscillations close to the energy minimum. The NA Hamiltonian, including the NA couplings and excitation energies, is iterated to model long time NAMD with the Pyxaid package. 1000 initial geometries are sampled from the MD trajectory to mimic the canonical distribution in the classical phase space. 500 random number sequences are used to sample the surface hopping probabilities for each initial geometry. The population and energy decay curves, Figures 4 and 5, represent averages over these NAMD trajectories. There are two trap states in the defective bilayer $MoTe_2$, see Figure 3(b). The population of defect state shown in Figure 4(b) is the sum of populations of the two defect levels. Pure phonon-driven trapping represented in Figure 5(a) takes sufficiently long time, providing enough time for electrons to relax between traps, such that most electrons are in the deep trap, releasing 0.3 eV of energy to phonons. On the other hand, phonon-suppressed Auger trapping, Figure 5(c), finishes in a short time, and ~67% of the trap electron populations is in the shallow trap. Thus, the trapped electron releases only ~0.2 eV of energy.

VI. Nonadiabatic Coupling (NAC)

In real-time time-dependent density functional theory (TDDFT), single-electron Kohn-Sham (KS) orbitals, $\Psi_n(\mathbf{r}, t)$, are used to express the electron density, $\rho(\mathbf{r}, t)$,

$\rho(\mathbf{r}, t) = \sum_{n=1}^{N_e} |\Psi_n(\mathbf{r}, t)|^2$ Equation S3.

where N_e represents the number of electrons. The equations-of-motion for the single-electron KS orbitals are obtained through applying the time-domain variational principle to the KS energy

$i\hbar \frac{\partial}{\partial t} \Psi_n(\mathbf{r}, t) = H(\mathbf{r}, \mathbf{R}, t) \Psi_n(\mathbf{r}, t)$ Equation S4.

Here, the Hamiltonian, $H(\mathbf{r}, \mathbf{R}, t)$, is time dependent due to the external potential created by the moving atoms **R**. The time-dependent KS orbitals, $\Psi_n(\mathbf{r}, t)$, are expanded in the basis of adiabatic KS orbitals, $\Phi_k(\mathbf{r}, \mathbf{R}(t))$, which are eigenstates of the KS Hamiltonian for the current atomic positions **R**.

$\Psi_n(\mathbf{r}, t) = \sum_k C_k^n(t) \Phi_k(\mathbf{r}, \mathbf{R}(t))$ Equation S5.

The nuclear trajectory $\mathbf{R}(t)$ is obtained from the MD simulation. Combination of eq 4 and eq 5 gives equations-of-motion for the expansion coefficients

$i\hbar \frac{\partial}{\partial t} C_j^n(t) = \sum_k C_k^n(t) (\varepsilon_k \delta_{jk} + d_{jk})$ Equation S6.

Here, ε_k is the energy of the adiabatic state k. d_{jk} is the nonadiabatic coupling (NAC) between adiabatic states k and j. NAC arises from the dependence of adiabatic wavefunctions, $\Phi_k(\mathbf{r}, \mathbf{R}(t))$, on the atomic motion **R.**

$d_{jk} = -i\hbar \langle \Phi_j | \nabla_{\boldsymbol{R}} | \Phi_k \rangle \cdot \frac{d\boldsymbol{R}}{dt} = -i\hbar \left\langle \Phi_j \middle| \frac{\partial}{\partial t} \middle| \Phi_k \right\rangle$ Equation S7.

In present, NAC is calculated numerically as the overlap between wave functions k and j at sequential time steps, according to the right-most part of the above equation. The many-particle formulation of the above formalism and implementation details are given in Ref 4[4].

VII. Pure Auger Trapping

In order to characterize the purely Auger charge trapping, we turned off the electron-phonon relaxation channel and repeated the calculations. Figure S6 presents the results of such calculations and compares them with the data obtained in the presence of both Auger and phonon-driven trapping channels. Compared with the Auger+phonon trapping process, the pure Auger trapping needs longer time, 2.8ps. In this case, the energy of trapped electron is used to excited the second electron higher into the CB. Note that the sum of the energies of the two electrons in Figure S6(d) is not conserved, because some of the energy is stored in off-diagonal terms of the Hamiltonian, in particular, in the NAC matrix elements computed in the two-electron basis. In comparison, during the Auger+phonon trapping process, about half of the trapped electron energy goes to excite the second electron, while the other half energy is deposited into phonons.

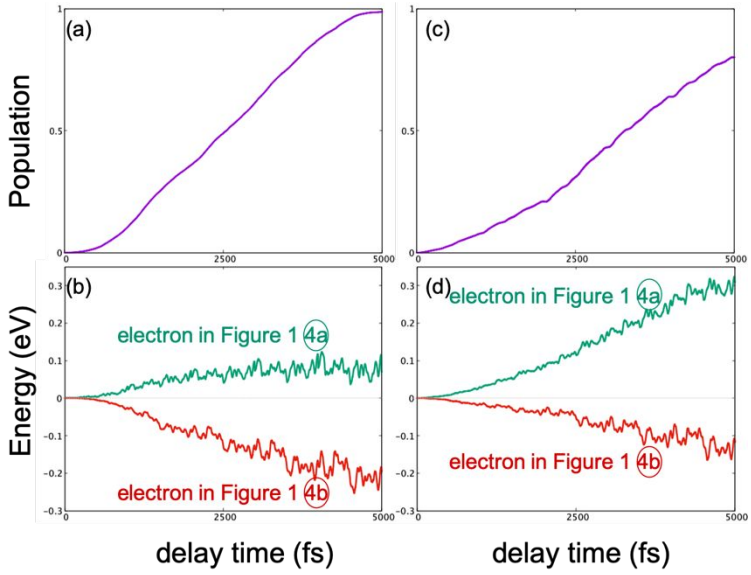

Figure S6. Population of trap states and changes in the energies of the two electrons during Auger trapping including (a,b) and excluding (c,d) the electron-phonon relaxation channel. Green curves depict energy of the second electron excited higher into the CB. Red curves depict energy of the trapped electron. Note that some of the energy is stored in off-diagonal NAC terms, such that the sum of the energies of the two electrons in (d) deviates from zero.

VIII. Defective $MoTe_2$ with Two Adjacent Te vacancies

High defect densities could create multiple mid-gap states some of which are close to band edges. Figure S7 depicts the DOS of $MoTe_2$ bilayer with two adjacent Te vacancies within one layer. In this system, multiple trap states appear close to the band edges. In such systems, phonon-driven charge trapping will be accelerated compared to the system with isolated defects. A faster phonon-driven trapping can compete effectively with Auger trapping, and suppress Auger trapping even more, providing further support to the conclusions of our work.

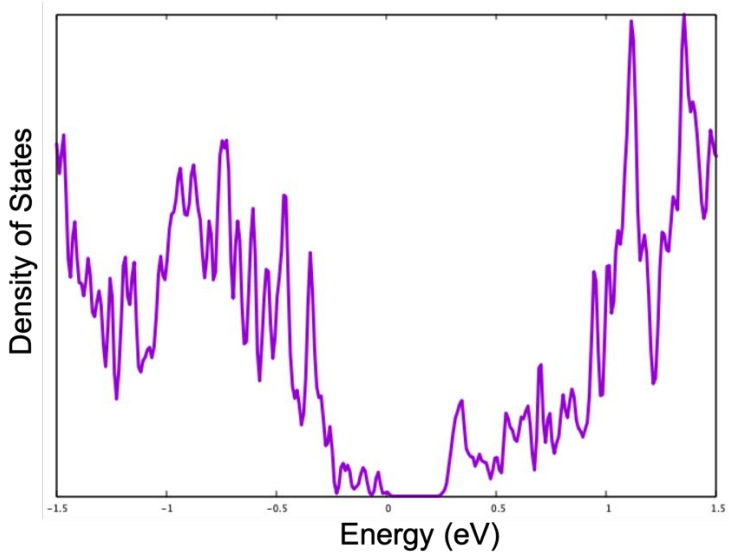

Figure S7. Density of states of defective $MoTe_2$ bilayer with two adjacent Te vacancies. Many trap states appear near band edges, facilitating fast phonon-trapping and further suppressing Auger trapping.

Supplementary References:

1. Zhang, X.; Jin, Z.; Wang, L.; Hachtel, J. A.; Villarreal, E.; Wang, Z.; Ha, T.; Nakanishi, Y.; Tiwary, C. S.; Lai, J.; Dong, L.; Yang, J.; Vajtai, R.; Ringe, E.; Idrobo, J. C.; Yakobson, B. I.; Lou, J.; Gambin, V.; Koltun, R.; Ajayan, P. M. Low Contact Barrier in 2H/1T′ MoTe2 In-Plane Heterostructure Synthesized by Chemical Vapor Deposition. *ACS Applied Materials & Interfaces* **2019,** 11, 12777-12785.

2. Heavens, O. S. Optical Properties of Thin Solid Films. *Dover Publications, INC. New York* **1965**.

3. Wang, K.; Feng, Y.; Chang, C.; Zhan, J.; Wang, C.; Zhao, Q.; Coleman, J. N.; Zhang, L.; Blau, W. J.; Wang, J. Broadband ultrafast nonlinear absorption and nonlinear refraction of layered molybdenum dichalcogenide semiconductors. *Nanoscale* **2014,** 6, 10530-10535.

4. Akimov, A. V.; Prezhdo, O. V. The PYXAID Program for Non-Adiabatic Molecular Dynamics in Condensed Matter Systems. *Journal of Chemical Theory Computation* **2013,** 9, 4959-4972.